ACS Photonics

Article

Cite This: ACS Photonics 2019, 6, 2213−2222

pubs.acs.org/journal/apchd5

Observation of Phonon Propagation in Germanium Nanowires Using Femtosecond Pump−Probe Microscopy

Erika M. Van Goethem, Christopher W. Pinion, Emma E. M. Cating, James F. Cahoon, and John M. Papanikolas*

Department of Chemistry, Caudill Laboratories, University of North Carolina at Chapel Hill, Chapel Hill 27599-3290, North Carolina, United States

Supporting Information

ABSTRACT: The excited-state dynamics in individual Ge nanowires (NWs) are imaged using ultrafast pump−probe microscopy with high spatial (∼600 nm) and temporal (∼500 fs) resolution. Photoexcitation of the NW by a focused femtosecond laser pulse promotes electrons from the valence band to the conduction band within a 400 nm segment of the 20−30 *μ*m long NW. The localized excitation is then probed by a delayed femtosecond pulse, whose position with respect to the pump pulse is precisely controlled. The pump−probe signals contain contributions from free carriers, thermal excitation, and impulsively excited acoustic phonons, the latter of which are detected in the time domain as a coherent oscillation in the pump−probe signal. Examination of an ensemble of NWs with diameters (*d*) ranging from 50 to 300 nm shows that the coherence frequency is inversely proportional to *d*, consistent with excitation of a radial breathing mode. In addition, experiments performed with spatially separated pump and probe beams show that the vibrational motion is not confined to the excitation region but, rather, spreads as much as 2.5 *μ*m along the NW axis during the first 3 ns after excitation. Spatially separated pump−probe microscopy also reveals the creation of a longitudinally propagating wave that travels along the NW at ∼6500 m/s or ∼20% faster than the speed of sound in bulk Ge.

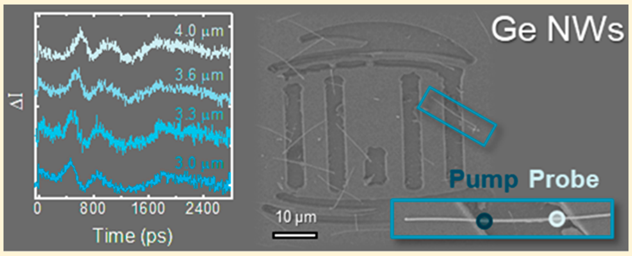

KEYWORDS: *Ultrafast Microscopy, Phonon Transport, Carrier Diffusion, Carrier Recombination, Thermal Conductivity*

Pump−probe experiments performed on semiconductor nanowires (NWs) often reflect a variety of dynamical phenomena, including carrier trapping, recombination, and thermal relaxation, as well as coherent processes arising from coherent excitation of lattice phonons. Size variation from one structure to the next complicates pump−probe signals obtained from ensembles of nanostructures, making it difficult to interpret them in terms of fundamental physical phenomena.[1,2] Even a first-order (or pseudo-first-order) kinetic process such as electron−hole recombination is observed as a multiexponential decay with a distribution of lifetimes that correspond to the range of diameters found in the ensemble.[1−5] The transient response arising from coherent excitation of acoustic phonons is also affected by this heterogeneity,[6] as slight variations in phonon frequencies due to different diameters causes dephasing and loss of the coherent signal over just a few vibrational periods.[7]

We used ultrafast pump−probe microscopy to circumvent this heterogeneity by performing transient transmission measurements on a single structure with diffraction-limited spatial resolution. Measurements performed using a spatially overlapped pump−probe (SOPP) configuration are analogous to conventional pump−probe spectroscopies but implemented in a microscopy mode. This configuration allows one to follow the excited-state dynamics from different structures, or different points within the same structure when an object is larger than the tightly focused pump and probe beams. Using this configuration, we discovered the presence of significant wire-to-wire variation in the surface recombination velocity (i.e., surface quality) in Si NWs, even when the NWs were selected from the same growth sample.[2] Work in our group also revealed strikingly different dynamics taking place at different points within individual nanostructures, including the partitioning between trap and band-edge electron−hole recombination in needle-shaped ZnO rods[8,9] and strain-induced recombination in bent Si NWs.[10] Measurements performed using a spatially separated pump−probe (SSPP) microscopy mode, in which independent scanning mechanisms for the two beams enable a structure to be excited in one location and probed in another, allow for the characterization of transport phenomena. We used this SSPP configuration to directly visualize the diffusion of photogenerated carriers[11] and the spread of thermal excitation in Si NWs,[12] as well as charge separation in Si NWs encoded with axial p-i-n junctions.[13]

Here, we report on the application of pump−probe microscopy methods to the study of Ge NWs. Like Si NWs, the transients obtained from Ge NWs include contributions

Received: December 17, 2018
Published: August 2, 2019

DOI: 10.1021/acsphotonics.8b01736
ACS Photonics 2019, 6, 2213−2222

from electron−hole recombination, carrier diffusion, and thermal relaxation. However, unlike Si, the Ge NWs also show clear evidence for impulsive excitation of acoustic modes. Low-frequency acoustic phonons have been observed in pump−probe transient absorption and microscopy experiments of many metals[14−27] and semiconductor nanostructures.[7,28,29] On the one hand, in the vast majority of these examples,[30,31] the nanostructures are smaller in size than the pump beam, thus generating a uniform excitation over the entire structure. The pump and probe spots in our experiment, on the other hand, are smaller than the NW length, resulting in phonon excitation in a localized segment of the wire. We observe two characteristic acoustic phonon modes. Coherent oscillations with a 10−20 ps period are observed at the location of the pump pulse, which we attribute to the excitation of a radial breathing mode (RBM) of the NW. The coherence persists for 3−5 ns, when the NW is mechanically decoupled from the substrate, and spatially separated experiments show that this excitation slowly spreads along the wire axis over many vibrational periods. Ultrafast excitation also creates a longitudinally propagating wave that is observed 3−5 μm away from the pump pulse as it travels along the NW at close to the speed of sound.

■ EXPERIMENTAL SECTION

NW Samples. Germanium NWs were grown with Au nanoparticle catalysts using the vapor−liquid−solid (VLS) mechanism,[32] using a home-built chemical vapor deposition (CVD) system[33] to produce single-crystal wires with a native oxide (GeOx) shell after exposure to ambient conditions. For a typical growth, 20.0 standard cubic centimeters (sccm) of germane gas was flowed through the reactor using 100 sccm of hydrogen as carrier gas, while maintaining a total reactor pressure of 30 Torr. The reactor was held at 320 °C for 5 min to nucleate wire growth and then cooled (60 °C/min) to 260 °C for continued wire growth over 1.5 h. The NWs were then dry-transferred from the growth chip to quartz substrates with trenches patterned by photolithography and formed by deep reactive ion etching. Pump−probe measurements were performed on suspended NW segments that span these trenches (5−15 μm wide), with several microns of the NW supported by the substrate on both sides, as well as segments supported entirely by the substrate. NWs were deposited on the registry patterned grid to relocate the exact NW in the scanning electron microscope (SEM) to correlate dynamics to structural features, such as NW diameter.

Ultrafast Microscope. Pump−probe experiments were performed with a home-built microscope based on a mode-locked Ti:sapphire laser.[11] In the setup, the 850 nm laser output is split by a 90:10 beam splitter, and the two beams pass through synchronized acousto-optic modulator (AOM) pulse pickers, reducing their repetition rates to 1.6 MHz. The more intense fraction is directed through a β-barium borate (BBO) crystal to generate the 425 nm pump pulse, while the lower-intensity component is used as the 850 nm probe. The probe is quadruple-passed through a 253 mm mechanical stage, providing ∼3.3 ns of optical delay. Access to pump−probe delays up to several hundred nanoseconds is achieved through the selection of different pulses from the 80 MHz pulse trains. The probe then passes through a set of computer-controlled scanning mirrors that change the angle of the beam as it enters the objective, allowing the probe to be focused to a spatially distinct point on the sample. The two beams are then attenuated using neutral density filters to 10 and 4 pJ/pulse for the pump and probe, respectively. They are then recombined using a dichroic mirror and directed onto the back aperture of a microscope objective (100×, 0.8 NA), which focuses the pump and probe beams to 400 and 600 nm diffraction-limited spots at the sample. Individual nanostructures are placed within the laser focus using a two-axis piezo scanning stage. The transmitted probe light is collected by a high numerical aperture (NA) condenser lens and detected by a balanced photodiode. The pump beam is modulated at 16 kHz, and the pump-induced changes in the probe intensity (ΔI) are detected by lock-in amplification. With this microscope, we can measure the transient response of a single nanostructure with ∼600 nm spatial resolution and ∼500 fs time resolution, with a sensitivity of $\Delta I/I \approx 1 \times 10^{-5}$.[9,11]

■ RESULTS AND DISCUSSION

Spatially overlapped pump−probe measurements on an individual Ge NW reveal a complex transient that has contributions from free carrier and thermal excitation, as well a low-frequency coherence arising from an acoustic phonon mode (Figure 1). This specific nanowire (denoted NW1) is ∼153 nm in diameter and is typical of the structures studied here. The pump pulse excites an ∼400 nm segment of the 20−30 μm long NW at the location indicated by the blue circle, promoting electrons from the valence band to the conduction band with a carrier density of ∼1×10^{20} cm^{-3}.[34] The photogenerated carriers alter the absorption and scattering properties of the Ge NW, causing the initial increase in the probe intensity (positive-going signal), which decays over time as the carriers undergo electron−hole recombination and migrate away from the point of excitation. The long-lived negative-going signal arises from localized heating of the NW by the pump pulse, which we estimate based on the amount of pump pulse energy deposited as thermal energy to be ∼150 K.[4,11,12,35,36] This component decays over time, as the thermal energy diffuses along the wire and dissipates into the substrate.[12] Superimposed on top of the free carrier and thermal contributions are time-dependent coherent oscillations that result from coherent excitation of a low-frequency radial breathing mode (RBM),[5,7,30,37,38] which could occur either

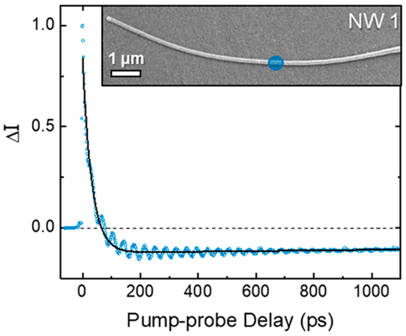

Figure 1. Transient obtained from a typical Ge nanowire (NW1) obtained with a spatially overlapped configuration. The NW is excited at 425 nm (10 pJ/pulse) at the location of the blue circle in the corresponding SEM image (inset) and probed by a delayed 850 nm laser pulse directed at the same location. The diameter of the blue circle approximates the spot size of the focused 425 nm pump pulse. The nanowire is 153 nm in diameter and supported on a quartz substrate. The black curve is the biexponential fit.

DOI: 10.1021/acsphotonics.8b01736
ACS Photonics 2019, 6, 2213−2222

through an impulsive or displacive mechanism.[39−42] The periodic vibrational motion of the NW modulates the transient signal, perhaps through strain-induced changes in the band structure or changes in refractive index.[5,7,27,43−48]

Free Carrier Relaxation and Thermal Dissipation Dynamics. The overall form of the transient depicted in Figure 1 (neglecting the coherent oscillations) is reasonably well-described by a biexponential form, that is

$$\Delta I(\Delta t) = A_{\mathrm{P}} \exp(-k_{\mathrm{P}}\Delta t) + A_{\mathrm{N}} \exp(-k_{\mathrm{N}}\Delta t) \tag{1}$$

where the first and second terms correspond to the loss of the photogenerated carrier population (positive-going component) and thermal energy within the probe spot (negative-going component), respectively. We note that, in this description, the decay rates (k_{P} = (32 ps)$^{-1}$ and k_{N} = (7.2 ns)$^{-1}$) have contributions from both population loss (i.e., recombination and heat dissipation) and transport (i.e., carrier migration and thermal diffusion), and thus, they are only effective rate constants.

Transport phenomena are probed directly by SSPP experiments. Displayed in Figure 2 are SSPP images depicting the spread of the photoexcitation in NW1 for time delays ranging from a few picoseconds to tens of nanoseconds.[11] The image at Δt = 0 ps shows the spatial distribution of the photoinduced transparency. Note that, because the size of the focused pump beam is larger than the diameter of the NW, the transparency appears to exceed the NW boundary, as indicated by the dashed lines in the figure. Over time this transparency spreads along the length of the NW, as the quasi-neutral charge cloud diffuses. During this time, the electrons and holes recombine, resulting in a fading of the photoinduced transparency, and by 88 ps, the images are dominated by the absorptive component (i.e., blue feature) that corresponds to a localized thermal excitation. This thermal component also spreads along the NW, but at a slower rate, and even at ∼2 ns it is only slightly larger than the initial excitation. By 30−40 ns the SSPP images show significant dispersal of the thermal excitation along the NW.

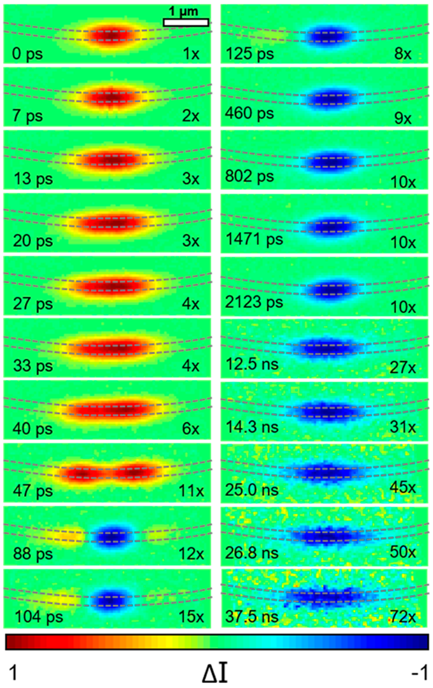

Figure 2. SSPP images from NW1. During the collection of these images, the location of the pump beam is held fixed and located at the point marked by the blue circle in the SEM image (Figure 1). The pump−probe delay is also fixed and held at the value indicated in the lower-left corner of each image. Each image is then obtained by raster scanning the probe beam across the field of view and collecting its pump-induced changes in intensity (i.e., ΔI). The intensity changes at each pixel, which reflects interaction with multiple pump−probe pulse pairs, are plotted on the normalized color table shown at the bottom of the figure, with relative scaling factors in the lower-right corner of the images. The pump pulse energy was 10 pJ/pulse. The NW location is denoted by the dashed lines.

When the population decays through higher-order kinetic processes, the center of the excitation region will decay faster than the wings, resulting in an apparent spatial broadening of the pump−probe signal that is not due to transport. However, at sufficiently low excitation intensities, the pump−probe kinetics are independent of the photoinjected carrier density. In this regime, the signal decays uniformly across the excitation region, and as a result, the observed spreading of the pump−probe signal is due only to transport. This situation leads to a separation of the spatiotemporal signal into two factors, one that describes the time evolution of the size of the pump−probe signal, and the other its temporal decay. The separation applies to both the free carrier and thermal signals, resulting in the following expression:[4,12,13]

$$\begin{aligned}\Delta I(\Delta t, \Delta x) = {}& \left[\alpha_{\mathrm{C}} \exp\left(\frac{-4 \ln 2\, \Delta x^2}{\Gamma_{\mathrm{C}}(\Delta t)^2}\right)\right]\left[\beta_{\mathrm{C}} \frac{\exp(-{}^{\Delta t}/_{\tau_{\mathrm{C}}})}{\Gamma_{\mathrm{C}}(\Delta t)}\right] \\ &+ \left[\alpha_{\mathrm{T}} \exp\left(\frac{-4 \ln 2\, \Delta x^2}{\Gamma_{\mathrm{T}}(\Delta t)^2}\right)\right]\left[\beta_{\mathrm{T}} \frac{\exp(-{}^{\Delta t}/_{\tau_{\mathrm{T}}})}{\Gamma_{\mathrm{T}}(\Delta t)}\right]\end{aligned} \tag{2}$$

where Δt and Δx are the temporal delay and spatial separation of the pump and probe spots along the nanowire, respectively. In this representation, the loss of the free carrier population and the dissipation of heat are modeled as first-order decay processes with corresponding lifetimes of τ_{C} and τ_{T}, respectively. The diffusional spreading of the free carrier and thermal signals along the NW are described by the Gaussian expressions with time-dependent full width at half-maximum (fwhm) values given by

$$\Gamma_{\mathrm{C}}(\Delta t) = \sqrt{{\gamma_{\mathrm{pu}}}^2 + {\gamma_{\mathrm{pr}}}^2 + 16 \ln 2\, D_{\mathrm{C}}\Delta t} \tag{3a}$$

$$\Gamma_{\mathrm{T}}(\Delta t) = \sqrt{{\gamma_{\mathrm{pu}}}^2 + {\gamma_{\mathrm{pr}}}^2 + 16 \ln 2\, D_{\mathrm{T}}\Delta t} \tag{3b}$$

where γ_{pu} and γ_{pr} are the fwhm sizes of the pump and probe spots (400 and 600 nm, respectively), D_{C} is the ambipolar diffusion constant for the free carriers, and D_{T} is the thermal diffusivity.

Overview of Kinetic Analysis. In principle, all four kinetic constants (τ_{C}, D_{C}, τ_{T}, D_{T}) could be obtained by fitting the set of SSPP images to these equations. However, global fits of this nature are not robust due to the structure of the spatiotemporal data sets. The SSPP images, for example, show the variation in the signal as a function of the pump−probe separation, but only for a sparse selection of time delays, while the SOPP transient shows how the signal varies with time delay, but only for a single overlap configuration. In addition, because the SSPP images are collected sequentially, the relative intensity between two images is known with less certainty when compared with two adjacent delay points in the SOPP transient, which are collected closer together in time and are thus less susceptible to instrumental drift.

Rather than pursue a global analysis of these equations using the entire data set, we take advantage of the separation of the transport and relaxation contributions and extract the four parameters through a two-step process. In the first step, we analyze the spread in the axial profile of SSPP images using the spatial portion of eq 2, that is

$$\Delta I(\Delta x;\ \Delta t) = \eta_{\mathrm{C},\Delta t}\ \exp\left(\frac{-4\ \ln 2\ \Delta x^2}{\Gamma_{\mathrm{C}}(\Delta t)^2}\right) + \eta_{\mathrm{T},\Delta t}\ \exp\left(\frac{-4\ \ln 2\ \Delta x^2}{\Gamma_{\mathrm{T}}(\Delta t)^2}\right) \tag{4}$$

where $\eta_{\mathrm{C},\Delta t} = \alpha_{\mathrm{C}}{\cdot}\beta_{\mathrm{C}}\ \exp(-\Delta t/\tau_{\mathrm{C}})/\Gamma_{\mathrm{C}}(\Delta t)$, and likewise for $\eta_{\mathrm{T},\Delta t}$. While $\eta_{\mathrm{C},\Delta t}$ and $\eta_{\mathrm{T},\Delta t}$ both depend upon Δt, for a given pump−probe delay they are constants, and the axial profile only depends upon the pump−probe separation Δx. By fitting eq 4 to the series of axial profiles, each collected at a different pump−probe delay, we can extract D_{C} and D_{T} without having to rely on an accurate measure of the relative signal intensities from one SSPP image to the next. Once D_{C} and D_{T} are determined, the lifetimes are then obtained by nonlinear least-squares fitting of $I(\Delta t) = I(\Delta t,0)$, that is

$$\Delta I(\Delta t) = \kappa_{\mathrm{C}}\frac{\exp\left(-{}^{\Delta t}\!/_{\tau_{\mathrm{C}}}\right)}{\Gamma_{\mathrm{C}}(\Delta t)} + \kappa_{\mathrm{T}}\frac{\exp\left(-{}^{\Delta t}\!/_{\tau_{\mathrm{Th}}}\right)}{\Gamma_{\mathrm{T}}(\Delta t)} \tag{5}$$

to the SOPP transient, where $\kappa_{\mathrm{C}} = \alpha_{\mathrm{C}}{\cdot}\beta_{\mathrm{C}}$, and similarly for κ_{T}. This decay expression reduces to a simple biexponential form in the limit that transport is slow compared to relaxation, a case that is not applicable here.

Transport Coefficients. Figure 3 depicts a series of axial profiles obtained from NW1. Each profile was generated by integrating the SSPP image normal to the NW axis (i.e., along the vertical direction in the panel). The positive-going profiles observed at early delays are dominated by the free-carrier signal and show clear lateral broadening, as the signal decays in amplitude (Figure 3A). By 40−50 ps, the impact of the thermal excitation becomes increasingly apparent, as the profile takes on a progressively more bimodal character. As the free carrier contribution disappears, all that remains is the negative-going thermal contribution, which at 460 ps has spread only slightly beyond the excitation region. While robust fits of eq 4 to the axial profiles are possible at intermediate time delays, where the two contributions are clear, at earlier times the thermal contribution causes only a slight distortion in the shape of the axial profile. This situation leads to a strong dependency between the amplitudes and widths of the two Gaussian components, and less stable fits.

We circumvent the problem by first determining the thermal diffusivity using the axial profiles from 460 ps to 37.5 ns (Figure 3B). Over this time range, the thermal signal measurably spreads along the wire axis. However, because the free carrier contribution has completely decayed, the profiles can be fit by a single Gaussian function. The set of six normalized profiles were simultaneously fit to eq 4 with $\eta_{\mathrm{C},\Delta t} = 0$ and $\eta_{\mathrm{T},\Delta t} = -1$. The fit treated D_{T} as a global fitting parameter and extracted a value of $D_{\mathrm{T}} = 0.2\ \mathrm{cm}^2/\mathrm{s}$. The thermal conductivity (k) is related to D_{T} by $k = \rho C_{\mathrm{p}} D_{\mathrm{T}}$, where ρ is the mass density ($5.32\ \mathrm{g/cm}^3$),[35] and C_{p} is the specific heat capacity ($0.32\ \mathrm{J/g{\cdot}K}$).[49] This expression yields $k = 29\ \mathrm{W/m{\cdot}K}$, which is approximately a factor of 2 smaller than the ~60 W/m·K value for bulk Ge.[50−52] A similar reduction in thermal conductivity between the NW and bulk forms is also observed in Si.[12] As with Si, the smaller conductivity in the NW is likely the result of a reduced mean free path of the high-frequency optical phonons responsible for thermal transport.

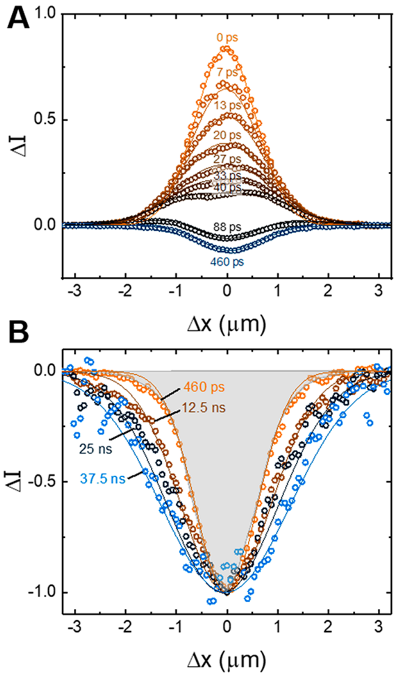

Figure 3. Quantifying thermal transport and carrier diffusion in NW1. The pump pulse energy was 10 pJ/pulse, and the excitation was located at the point marked by the blue circle in the SEM image (Figure 1). (A) Axial profiles depicting the spatial distribution of the pump−probe signal along NW1 during the first 460 ps after excitation. In this time window, the axial profile evolves from a photoinduced transparency at zero delay to a photoinduced absorption at 460 ps. (B) SSPP axial profiles for delays ranging from 460 ps to 37.5 ns. Each profile is normalized to −1, and the gray shaded region shows the size of the initial excitation.

The free carrier diffusion constant (D_{C}) is determined through a simultaneous fitting of eq 4 to the 10 SSPP axial profiles obtained during the first 125 ps after excitation. The fit is constrained by treating $D_{\mathrm{T}} = 0.2\ \mathrm{cm}^2/\mathrm{s}$ as a fixed parameter. The fit is further constrained by determining the amplitudes for the free carrier and thermal components ($B_{\mathrm{C},\Delta t}$ and $B_{\mathrm{T},\Delta t}$, respectively) at each delay using the results of the biexponential fit to the SOPP transient (Figure 1) and then setting them to be fixed parameters, as well. Thus, the only adjustable parameter in the global fit of eq 4 to the SSPP axial profiles is D_{C}. The best fit to the data is obtained when $D_{\mathrm{C}} = 63.2\ \mathrm{cm}^2/\mathrm{s}$, which is comparable to the value observed in bulk Ge.[53,54]

Lifetimes. The SOPP transient depicted in Figure 1 is fit using eq 5 with $D_{\mathrm{C}} = 63.2\ \mathrm{cm}^2/\mathrm{s}$ and $D_{\mathrm{T}} = 0.2\ \mathrm{cm}^2/\mathrm{s}$, $\tau_{\mathrm{C}} = 46$ ps, and $\tau_{\mathrm{T}} = 9.0$ ns. Both are longer than the observed lifetimes (k_{N}^{-1} and k_{P}^{-1}) extracted from the biexponential fit, which are influenced by transport processes, as discussed above. Electron−hole recombination in nanostructures can occur through a combination of mechanisms, including surface-mediated mechanisms, as well as higher-order processes such as Auger recombination that occur in the NW core.[3]

Transients collected at a series of excitation intensities show that the lifetime is nearly constant for pump pulse energies up to ~5 pJ, after which it becomes shorter with increasing intensity. Thus, while recombination is likely dominated by surface-mediated processes, there appears to be a slight enhancement of the recombination rate at 8−10 pJ (and higher) due to higher-order kinetic processes. The effects of Auger recombination are also reported in ensemble pump−probe measurements performed on Ge NWs at similar excitation intensities,[5,7] consistent with our observations. The carrier recombination time in Ge NWs is markedly faster than that observed in Si NWs, which exhibit carrier lifetimes of 200−500 ps for NWs of comparable diameter.

Phonon Dynamics. Shown in Figure 4 are SOPP transients obtained from a 125 nm diameter Ge NW suspended across a 5 μm trench etched into a quartz substrate. Two transient data sets are shown in Figure 4A, one from the section suspended over the trench and the other from a segment in contact with the quartz substrate. Both traces were fit to eq 5, and the resulting fit residuals, which isolate the coherent amplitude oscillations, are depicted in Figure 4B. While the free carrier and thermal contributions are largely unaffected by decoupling the NW from the substrate, suspending the NW increases the amplitude of the coherent signal and extends its lifetime by as much as a factor of 6 compared to the section in contact with the substrate (Figure 4B). Fourier transform (FT) of the residuals yields the phonon frequency spectra depicted in Figure 4C. While both sections of the NW show an intense frequency component near 30 GHz, there appears to be a slight upshift in the RBM frequency when the NW is in contact with the substrate, which perhaps reflects the presence of a restitutive force that increases the RBM frequency.

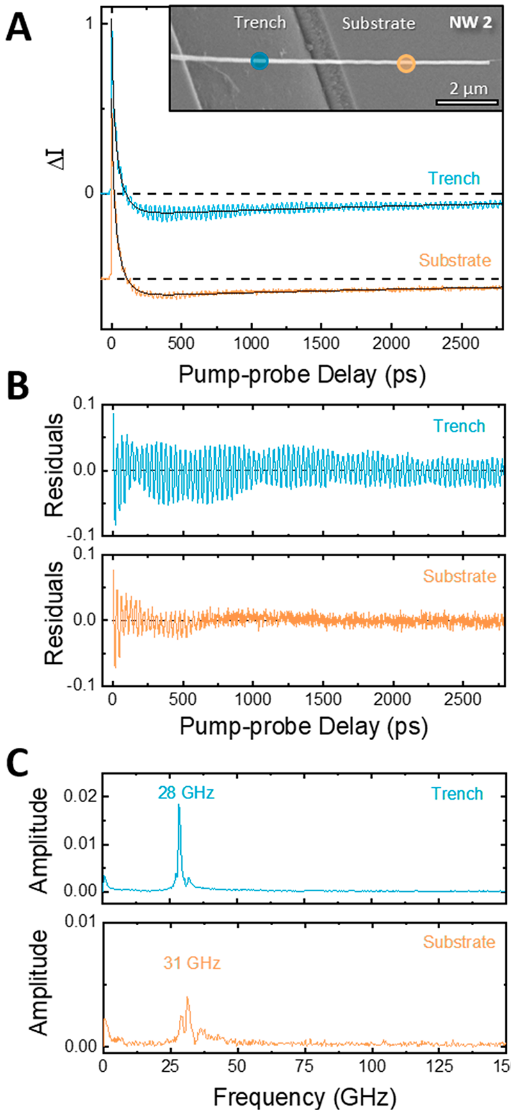

Figure 4. (A) SOPP kinetic traces obtained from substrate-supported (orange) and suspended (blue) sections of NW2. Solid black lines are best fits to eq 5. (inset) The SEM image with the trench (left) and substrate (right) visible. The positions at which transient scans were collected are highlighted by blue and orange circles, whose diameters approximate the spot size of the focused pump beam. (B) Residuals from fitting yields coherent oscillations. (C) Frequency spectrum obtained by FT of residuals.

Pump−probe measurements performed on multiple NWs (Figure S2 in Supporting Information) show that the coherence frequency increases with decreasing diameter, much in the same way that the pitch of a bell changes with size. This variation with diameter is exemplified by the data from the two NWs depicted in Figure 5A. There is a clear increase in the coherence period for the larger of the two nanowires (Figure 5B), and Fourier analysis reveals that the RBM frequency decreases by a factor of 2 as the diameter increases from 123 to 220 nm (Figure 5C). Pump−probe measurements performed on an ensemble of NWs provide a quantitative relationship between vibrational frequency and NW size. RBM frequencies obtained from 38 different locations on 24 different NWs with diameters ranging from 50 to 300 nm (as measured by SEM) show that the coherence frequency scales linearly with $1/d$ (Figure 5D, with labeled data points in Figure S1 in Supporting Information).

The inverse proportionality with diameter is consistent with elastomeric models of the NW. The RBM frequency (ω_{br}) predicted for an isotropic elastic cylinder is given by

$$\omega_{\mathrm{br}}^{(n)} = \frac{\xi_n}{\pi d} C_{\mathrm{L}} \tag{6}$$

In this expression, d is the NW diameter, C_{L} is the longitudinal speed of sound,[27,57] and ξ_n is the nth eigenvalue obtained from

$$\xi_n J_0(\xi_n) = \frac{1-2\nu}{1-\nu} J_1(\xi_n) \tag{7}$$

where ν is the Poisson ratio, and $J_0(\xi)$ and $J_1(\xi)$ are Bessel functions. For Ge, $\nu = 0.28$,[56] which yields $\xi_0 = 2.10$ and $\xi_1 = 5.41$ for the fundamental and first overtone, respectively. The frequencies for the fundamental and first overtone obtained from eq 6 with $C_{\mathrm{L}} = 5400$ m/s (speed of sound in bulk Ge)[58] are depicted as a function of NW diameter by the dashed lines in Figure 5C.

The fundamental frequency ($n = 0$) closely matches the most prominent frequency component observed in the phonon spectrum. Some structures (e.g., NW3) also show a very weak higher-frequency peak that could correspond to the first overtone ($n = 1$) of the RBM. While the agreement with this elastic cylinder model is remarkable, when parametrized using C_{L} and ν values for bulk Ge, it appears to slightly underestimate the RBM frequencies observed in the NW ensemble. While origin of this deviation is unclear, it is possible that these properties in the NW differ somewhat from those of

DOI: 10.1021/acsphotonics.8b01736
ACS Photonics 2019, 6, 2213−2222

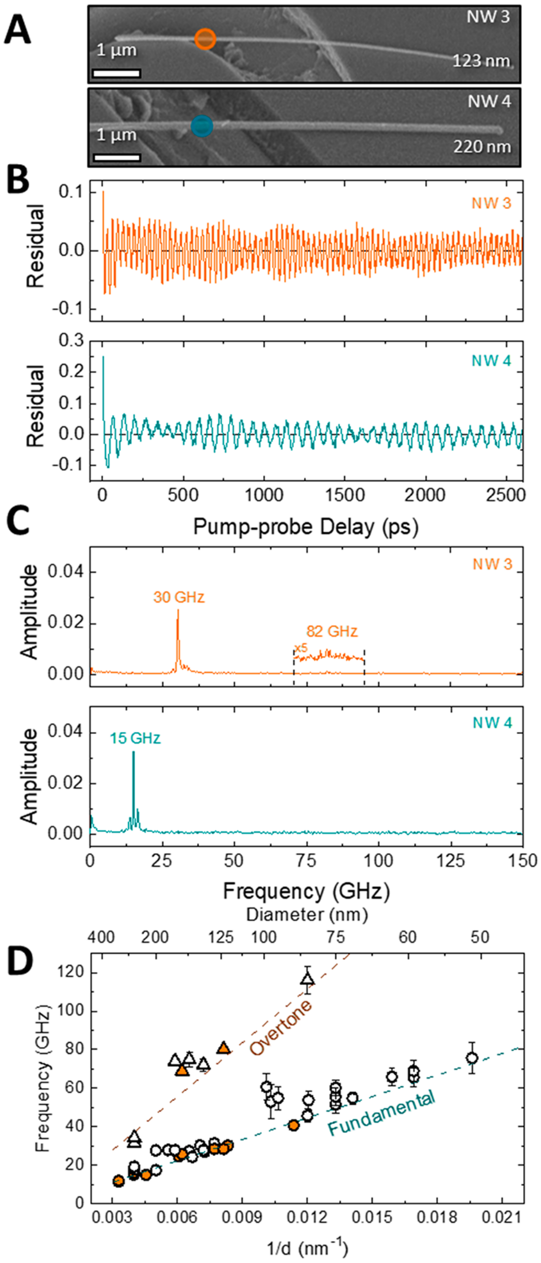

Figure 5. Diameter dependence of acoustics phonon mode. (A) SEM images of suspended NW3 and NW4. (B) Coherence patterns (residuals from fitting the transient signals) corresponding to the NW3 (orange) and NW4 (teal). Orange and teal circles in the SEM images depict the locations where transient scans were collected, and their diameters approximate the spot size of the focused pump beam. (C) Frequency spectrum obtained by FT of the coherence patterns for NW3 and NW4. The spectra show the fundamental modes at 30 GHz (NW3, d = 123 nm) and 15 GHz (NW4, d = 220 nm) and the first overtone mode at 82 GHz in NW3. (D) The frequency of the observed vibrational modes versus $1/d$. The symbols represent experimental data, with the orange and white filled symbols showing measurements performed on suspended and substrate-supported NW sections, respectively. Dashed lines represent calculations for fundamental (teal) and first overtone breathing modes (orange) (ξ_0 = 2.10 and ξ_1 = 5.41), performed using the bulk elastic constants of germanium.[55,56] Error bars represent the fwhm of the RBM peaks in the phonon spectra. Error bars smaller than the symbols were omitted for clarity.

the bulk. Indeed, better agreement can be achieved either by increasing the value of C_L to ∼6000 m/s or the value of ν to ∼0.45. Another possibility is that this deviation results from a substrate-induced alteration of the RBM frequency. The collection of data points in Figure 5D represent data collected from both suspended sections and substrate-supported segments of the NWs, with the symbols representing the suspended segments highlighted by the orange fill. Although there are only nine measurements on suspended sections depicted in the figure, the RBM frequencies observed at those locations exhibit better agreement with this elastomeric model, suggesting that the observation of values that exceed the theoretical prediction could be due to the presence of the substrate.

Close examination of the SOPP transients shows a clear beat pattern in the coherence component that gives rise to satellite peaks in the phonon spectrum. Similar beating is observed in transient signals of metal nanowires,[26,27,59] where the noncircular cross section gives rise to multiple RBMs with similar frequencies that interfere with each other.[26,60] While the physical origin of the satellite peaks in the Ge NWs is not entirely clear, it appears that they may correlate with the NW diameter, with larger NWs tending to exhibit a single RBM feature in their phonon spectra (see Supporting Information). Although we have a limited sampling, the appearance of the satellite peaks in the phonon spectra of the smaller Ge NWs could indicate that the modulated amplitude of the coherence in their transients arises from a similar beating between closely spaced modes resulting from a slightly noncircular NW cross section.

Spreading of the phonon excitation along the NW is observed by collecting transients with spatially separated pump and probe beams (Figure 6). The experimental geometry is depicted in Figure 6A, which shows NW5 suspended across a 5 μm wide trench. The pump beam is directed onto the NW near one edge of the trench (red circle), impulsively exciting a localized region of the NW. The probe beam (purple circle) is then positioned at a distance (Δx) away, toward the opposite side of the trench. Figure 6B shows a series of 13 transients obtained at increasing separations (Δx) ranging from 0 to 4 μm, with the different probe locations marked by the arrows in Figure 6A. The transient obtained when the pump and probe are spatially coincident (Δx = 0) exhibits the same dynamical features as the transient observed for NW1 (Figure 1) and NW2 (Figure 3). The shape of the transients changes dramatically as the probe pulse is moved progressively further away from the pump. There is an overall decrease in the pump−probe signal, the magnitude of which is indicated by the scaling factors shown at the right for each transient. The transients obtained with Δx between 1.0 and 1.7 μm show a delayed rise in the signal, reflecting the time needed for charge carriers to reach the location of the probe beam. Given the spot sizes of the pump and probe beams (400 and 600 nm, respectively), there is some residual overlap of the two laser pulses for separations up to ∼1.0 μm, which is likely the reason for the observation of signal at Δt = 0 ps. For larger separations, their spatial overlap is expected to be negligible, yet we still observe pump−probe signal at Δt = 0 ps, even at separations as large as 4 μm. We do not observe this type of prompt signal in experiments where the NW is in direct contact with the substrate, suggesting that its origin involves the trench geometry of the experiment. One possibility is that it results from scattering of the pump beam by the trench as it

DOI: 10.1021/acsphotonics.8b01736
ACS Photonics 2019, 6, 2213−2222

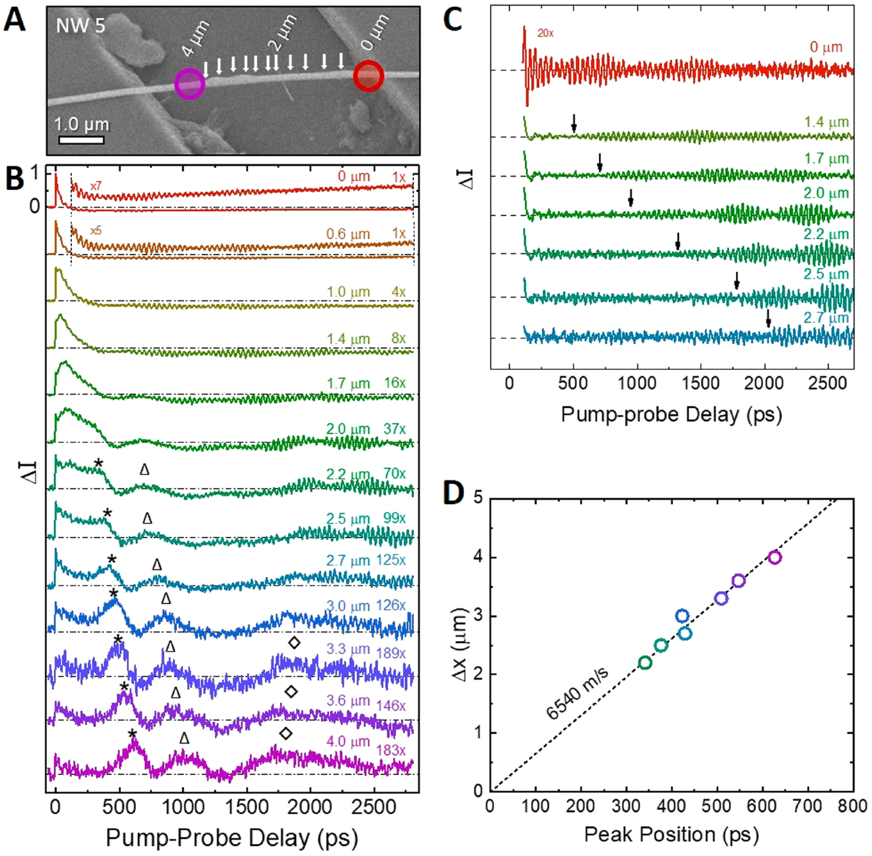

Figure 6. SSPP transients depicting an acoustic phonon propagation. (A) SEM image showing suspended section of NW5. The location of the pump excitation is indicated by red circle. The probe position is displaced from the pump along the NW axis up to 4 μm separation (purple circle) in steps of ~200−400 nm as denoted by the arrows. The diameters of the red and purple circles approximate the fwhm size of the pump and probe beams. (B) SSPP transients obtained with the pump−probe separations Δx between 0 and 4 μm. Each transient is normalized to its maximum signal with scaling factors relative to $\Delta x = 0$ μm shown to the right. The asterisk, triangle, and diamond symbols mark three recurrences in the transient signal that result from excitation of a low-frequency mode propagating out from the point of excitation. (C) Pump−probe transients after application of a high-pass Fourier filter show delayed onset of high-frequency coherence at larger separations, as indicated by arrows above each trace. (D) The spatial position of the fundamental phonon peak (marked by asterisks in (B)) vs pump−probe delay. The slope of the linear fit line (black) is the propagation speed of the low-frequency mode.

passes through the sample, causing a weak excitation of the NW even at the remote locations.

Like the free carrier and thermal signals, the coherence associated with the RBM also appears to exhibit a delayed onset when the pump and probe spots are well-separated. The RBM coherence in the SSPP transients is isolated through application of high-pass Fourier filter, which removes frequency components below 10 GHz (Figure 6C). This delayed onset (marked by the arrows in the figure) is apparent when the separation exceeds 1.0 μm, although it is most easily seen in the $\Delta x = 2.0$−2.5 μm transients, where the coherent oscillations do not appear until ~1000 ps (or later) and then increase in amplitude over time. As the separation is further increased, it takes more time for the signature of the RBM to appear, and by 2.7 μm the onset of the coherent oscillation has shifted beyond the 2.8 ns time window of the experiment. The systematic delay in the coherence onset at larger separations indicates that the RBM motion is not confined to the point of excitation but rather slowly spreads along NW axis at ~1 nm/ps, as the expansion and contraction of the NW in one location induces vibrational motion in adjacent sections that are initially vibrationally quiet.

The series of transients also show a broad temporal feature (marked by an asterisk) that is first noticeable as a shoulder in the 2.2 μm transient at ~350 ps. This feature is followed by a second recurrence of weaker intensity (marked by the triangle) appearing at ~750 ps. The arrival time of these two features increases linearly with pump−probe separation (Figure 6D), indicating the transient distortion moves at a constant velocity away from the point of excitation. We attribute these two features to the formation of a wave propagating longitudinally along the NW axis at ~6540 m/s, or ~20% faster than the speed of sound in bulk germanium (5400 m/s).[61] Measurements performed on NW9 show a similar propagating wave but with a slightly slower speed of 6040 m/s (Figure S3 in Supporting Information).

The coherence period (T), or time between successive recurrences, can be written in terms of the propagation velocity (V_g) and its wavelength (Λ) as $T = \Lambda/V_g$. Taking Λ to be approximately twice the size of the excitation region (i.e., $\Lambda = 2\cdot 2.5\ \gamma_{pu}$) yields $\Lambda \approx 2.0$ μm, which in turn gives $T \approx 310$ ps, a value that is comparable to the 400 ps observed in the SSPP transients. This simple analysis indicates that the oscillation period and wavelength of the propagating wave are determined by the spatial extent of the excitation, much in the same way that vibrational frequency depends on the grating period in impulsive stimulated Brillouin scattering (ISBS) experiments.[45,62] However, in those experiments, the transient grating formed by the crossed pump beams forms a well-defined spatial wave in the material, resulting in a long-lived coherence. Since the pump excitation is spatially localized, this wave is not described by a single wavelength but rather a superposition of waves, resulting in a short coherence time and the observation of only two recurrences in the pump−probe signal.

These two features are followed by a third recurrence in the signal (marked by a diamond) that is significantly broader than the other features. This third recurrence is most well-defined at the largest separation (4 μm), arriving at 2−3 ns after excitation. However, whereas the arrival of the first two features is increasingly delayed as the probe is moved away from the pump, the third appears to arrive earlier and becomes more intense at the furthest separation. These observations might suggest that the third recurrence results when the propagating wave reaches the far side of the trench and reflects off the point where the NW contacts the substrate. The reflected wave would then travel back along the NW toward the location of the probe pulse, which would take longer to reach when the probe spot is located closer to the pump (i.e., smaller Δx). While this scenario accounts for the timing of the third recurrence, we note that this feature is not significantly attenuated relative to the second recurrence, as one might expect, and we do not observe strong evidence of this reflected wave in the SSPP data collected on NW9 (Figure S3 in Supporting Information), although a third recurrence is evident. Nevertheless, further investigation of the phenomena using samples with better defined contacts may shed light on the matter.

■ CONCLUSIONS

In summary, the pump pulse photoexcites electron−hole pairs within a localized section of the Ge NW. Rapid electron−hole recombination results in a coherent excitation of an RBM and a longitudinally propagating wave. When the NW is in contact with the substrate, the coherences dampen out quickly. Suspending the NW across a trench reduces its mechanical coupling with the substrate, allowing the coherence to live much longer. We observe spreading of the RBM outside the initial excitation spot at a rate of ∼1 nm/ps. The longitudinally propagating wave travels along the NW axis at ∼6500 m/s. Time-resolved images show clear evidence of rapid diffusion and recombination of the free carriers followed by thermal transport on slower time scales. Charge-carrier diffusion is similar to that observed in bulk Ge; the thermal diffusion is ∼2× slower than the bulk, consistent with trends previously observed in our studies of Si NWs.

■ ASSOCIATED CONTENT

Ⓢ Supporting Information

The Supporting Information is available free of charge on the ACS Publications website at DOI: 10.1021/acsphotonics.8b01736.

> Data for all NWs studied, including SEM images, SOPP transients, residuals from fits, and phonon spectra, as well as an analysis of the satellite peaks in the phonon spectra (PDF)

■ AUTHOR INFORMATION

Corresponding Author

*E-mail: john_papanikolas@unc.edu.

ORCID

Erika M. Van Goethem: 0000-0002-3360-9520
Emma E. M. Cating: 0000-0001-6040-5622
James F. Cahoon: 0000-0003-1780-215X
John M. Papanikolas: 0000-0002-0902-6990

Author Contributions

The manuscript was written through the contributions of all authors. All authors have given approval to the final version of the manuscript.

Notes

The authors declare no competing financial interest.

■ ACKNOWLEDGMENTS

This work was supported by the National Science Foundation (NSF) under Grant Nos. CHE-1464776 and later CHE-1764228 (E.M.V., E.M.C., and J.M.P.), as well as DMR-1555001 (C.W.P. and J.F.C.). E.M.V. acknowledges an NC Space Grant graduate research fellowship. C.W.P. acknowledges an NSF Graduate Research Fellowship. J.F.C. acknowledges a Packard Fellowship for Science and Engineering. This work was performed in part at the Chapel Hill Analytical and Nanofabrication Laboratory, a member of the North Carolina Research Triangle Nanotechnology Network, which is supported by the NSF, Grant No. ECCS-1542015, as part of the Nanotechnology Coordinated Infrastructure.

■ REFERENCES

(1) Grumstrup, E. M.; Cating, E. M.; Gabriel, M. M.; Pinion, C. W.; Christesen, J. D.; Kirschbrown, J. R.; Vallorz, E. L.; Cahoon, J. F.; Papanikolas, J. M. Ultrafast Carrier Dynamics of Silicon Nanowire Ensembles: The Impact of Geometrical Heterogeneity on Charge Carrier Lifetime. *J. Phys. Chem. C* **2014**, *118*, 8626−8633.

(2) Cating, E. E. M.; Pinion, C. W.; Christesen, J. D.; Christie, C. A.; Grumstrup, E. M.; Cahoon, J. F.; Papanikolas, J. M. Probing Intrawire, Interwire, and Diameter-Dependent Variations in Silicon Nanowire Surface Trap Density with Pump-Probe Microscopy. *Nano Lett.* **2017**, *17*, 5956−5961.

(3) Prasankumar, R. P.; Choi, S.; Trugman, S. A.; Picraux, S. T.; Taylor, A. J. Ultrafast Electron and Hole Dynamics in Germanium Nanowires. *Nano Lett.* **2008**, *8*, 1619−1624.

(4) Grumstrup, E. M.; Gabriel, M. M.; Cating, E. M.; Pinion, C. W.; Christesen, J. D.; Kirschbrown, J. R.; Vallorz, E. L.; Cahoon, J. F.; Papanikolas, J. M. Ultrafast Carrier Dynamics in Individual Silicon Nanowires: Characterization of Diameter-Dependent Carrier Lifetime and Surface Recombination with Pump−Probe Microscopy. *J. Phys. Chem. C* **2014**, *118*, 8634−8640.

(5) Li, Y.; Clady, R.; Park, J.; Thombare, S. V.; Schmidt, T. W.; Brongersma, M. L.; McIntyre, P. C. Ultrafast electron and phonon response of oriented and diameter-controlled germanium nanowire arrays. *Nano Lett.* **2014**, *14*, 3427−31.

(6) Hu, M.; Hillyard, P.; Hartland, G. V.; Kosel, T.; Perez-Juste, J.; Mulvaney, P. Determination of the elastic constants of gold nanorods produced by seed mediated growth. *Nano Lett.* **2004**, *4*, 2493−2497.

(7) Li, Y.; Clady, R.; Marshall, A. F.; Park, J.; Thombare, S. V.; Chan, G.; Schmidt, T. W.; Brongersma, M. L.; McIntyre, P. C. Ultrafast Carrier Dynamics of a Photo-Excited Germanium Nanowire−Air Metamaterial. *ACS Photonics* **2015**, *2*, 1091−1098.

(8) House, R. L.; Mehl, B. P.; Kirschbrown, J. R.; Barnes, S. C.; Papanikolas, J. M. Characterizing the Ultrafast Charge Carrier Trapping Dynamics in Single ZnO Rods Using Two-Photon Emission Microscopy. *J. Phys. Chem. C* **2011**, *115*, 10806−10816.

(9) Mehl, B. P.; Kirschbrown, J. R.; Gabriel, M. M.; House, R. L.; Papanikolas, J. M. Pump-probe microscopy: spatially resolved carrier dynamics in ZnO rods and the influence of optical cavity resonator modes. *J. Phys. Chem. B* **2013**, *117*, 4390−8.

(10) Grumstrup, E. M.; Gabriel, M. M.; Pinion, C. W.; Parker, J. K.; Cahoon, J. F.; Papanikolas, J. M. Reversible strain-induced electron-hole recombination in silicon nanowires observed with femtosecond pump-probe microscopy. *Nano Lett.* **2014**, *14*, 6287−92.

(11) Gabriel, M. M.; Kirschbrown, J. R.; Christesen, J. D.; Pinion, C. W.; Zigler, D. F.; Grumstrup, E. M.; Mehl, B. P.; Cating, E. E.; Cahoon, J. F.; Papanikolas, J. M. Direct imaging of free carrier and trap carrier motion in silicon nanowires by spatially-separated femtosecond pump-probe microscopy. *Nano Lett.* **2013**, *13*, 1336−40.

(12) Cating, E. E.; Pinion, C. W.; Van Goethem, E. M.; Gabriel, M. M.; Cahoon, J. F.; Papanikolas, J. M. Imaging Spatial Variations in the Dissipation and Transport of Thermal Energy within Individual Silicon Nanowires Using Ultrafast Microscopy. *Nano Lett.* **2016**, *16*, 434−9.

(13) Gabriel, M. M.; Grumstrup, E. M.; Kirschbrown, J. R.; Pinion, C. W.; Christesen, J. D.; Zigler, D. F.; Cating, E. E.; Cahoon, J. F.; Papanikolas, J. M. Imaging charge separation and carrier recombination in nanowire p-i-n junctions using ultrafast microscopy. *Nano Lett.* **2014**, *14*, 3079−87.

(14) Lo, S. S.; Major, T. A.; Petchsang, N.; Huang, L.; Kuno, M. K.; Hartland, G. V. Charge Carrier Trapping and Acoustic Phonon Modes in Single CdTe Nanowires. *ACS Nano* **2012**, *6*, 5274−5282.

(15) Zijlstra, P.; Tchebotareva, A. L.; Chon, J. W. M.; Gu, M.; Orrit, M. Acoustic Oscillations and Elastic Moduli of Single Gold Nanorods. *Nano Lett.* **2008**, *8*, 3493−3497.

(16) Staleva, H.; Skrabalak, S. E.; Carey, C. R.; Kosel, T.; Xia, Y.; Hartland, G. V. Coupling to light, and transport and dissipation of energy in silver nanowires. *Phys. Chem. Chem. Phys.* **2009**, *11*, 5889−5896.

(17) Juve, V.; Crut, A.; Maioli, P.; Pellarin, M.; Broyer, M.; Del Fatti, N.; Vallee, F. Probing elasticity at the nanoscale: Terahertz acoustic vibration of small metal nanoparticles. *Nano Lett.* **2010**, *10*, 1853−8.

(18) Polli, D.; Lisiecki, I.; Portalès, H.; Cerullo, G.; Pileni, M.-P. Low Sensitivity of Acoustic Breathing Mode Frequency in Co Nanocrystals upon Change in Nanocrystallinity. *ACS Nano* **2011**, *5*, 5785−5791.

(19) Yu, K.; Zijlstra, P.; Sader, J. E.; Xu, Q. H.; Orrit, M. Damping of acoustic vibrations of immobilized single gold nanorods in different environments. *Nano Lett.* **2013**, *13*, 2710−6.

(20) Jean, C.; Belliard, L.; Cornelius, T. W.; Thomas, O.; Pennec, Y.; Cassinelli, M.; Toimil-Molares, M. E.; Perrin, B. Spatiotemporal Imaging of the Acoustic Field Emitted by a Single Copper Nanowire. *Nano Lett.* **2016**, *16*, 6592−6598.

(21) Jean, C.; Belliard, L.; Cornelius, T. W.; Thomas, O.; Toimil-Molares, M. E.; Cassinelli, M.; Becerra, L.; Perrin, B. Direct Observation of Gigahertz Coherent Guided Acoustic Phonons in Free-Standing Single Copper Nanowires. *J. Phys. Chem. Lett.* **2014**, *5*, 4100−4.

(22) Petrova, H.; Perez Juste, J.; Pastoriza-Santos, I.; Hartland, G. V.; Liz-Marzan, L. M.; Mulvaney, P. On the temperature stability of gold nanorods: comparison between thermal and ultrafast laser-induced heating. *Phys. Chem. Chem. Phys.* **2006**, *8*, 814−21.

(23) Hu, M.; Wang, X.; Hartland, G. V.; Mulvaney, P.; Juste, J. P.; Sader, J. E. Vibrational response of nanorods to ultrafast laser induced heating: theoretical and experimental analysis. *J. Am. Chem. Soc.* **2003**, *125*, 14925−33.

(24) Hartland, G. V. Optical studies of dynamics in noble metal nanostructures. *Chem. Rev.* **2011**, *111*, 3858−87.

(25) Jellison, G. E. Optical functions of GaAs, GaP, and Ge determined by two-channel polarization modulation ellipsometry. *Opt. Mater.* **1992**, *1*, 151−160.

(26) Yu, K.; Major, T. A.; Chakraborty, D.; Devadas, M. S.; Sader, J. E.; Hartland, G. V. Compressible Viscoelastic Liquid Effects Generated by the Breathing Modes of Isolated Metal Nanowires. *Nano Lett.* **2015**, *15*, 3964−70.

(27) Major, T. A.; Lo, S. S.; Yu, K.; Hartland, G. V. Time-Resolved Studies of the Acoustic Vibrational Modes of Metal and Semiconductor Nano-objects. *J. Phys. Chem. Lett.* **2014**, *5*, 866−74.

(28) Sakuma, H.; Tomoda, M.; Otsuka, P. H.; Matsuda, O.; Wright, O. B.; Fukui, T.; Tomioka, K.; Veres, I. A. Vibrational modes of GaAs hexagonal nanopillar arrays studied with ultrashort optical pulses. *Appl. Phys. Lett.* **2012**, *100*, 131902.

(29) Latham, W. P.; Smirl, A. L.; Elci, A.; Bessey, J. S. The role of phonons and plasmons in describing the pulsewidth dependence of the transmission of ultrashort optical pulses through germanium. *Solid-State Electron.* **1978**, *21*, 159−165.

(30) Sokolowski-Tinten, K.; Shymanovich, U.; Nicoul, M.; Blums, J.; Tarasevitch, A.; Horn-von-Hoegen, M.; von der Linde, D.; Morak, A.; Wietler, T. In *Energy relaxation and anomalies in the thermo-acoustic response of femtosecond laser-excited Germanium;* Springer Berlin Heidelberg: Berlin, Germany, 2007; pp 597−599.

(31) Dong, S.; Lian, J.; Jhon, M. H.; Chan, Y.; Loh, Z. H. Pump-Power Dependence of Coherent Acoustic Phonon Frequencies in Colloidal CdSe/CdS Core/Shell Nanoplatelets. *Nano Lett.* **2017**, *17*, 3312−3319.

(32) Prasankumar, R. P.; Upadhya, P. C.; Taylor, A. J. Ultrafast carrier dynamics in semiconductor nanowires. *Phys. Status Solidi B* **2009**, *246*, 1973−1995.

(33) Pinion, C. W.; Nenon, D. P.; Christesen, J. D.; Cahoon, J. F. Identifying Crystallization- and Incorporation-Limited Regimes During Vapor−Liquid−Solid Growth of Si Nanowires. *ACS Nano* **2014**, *8*, 6081−6088.

(34) Zollner, S.; Myers, K. D.; Jensen, K. G.; Dolan, J. M.; Bailey, D. W.; Stanton, C. J. Femtosecond interband hole scattering in Ge studied by pump-probe reflectivity. *Solid State Commun.* **1997**, *104*, 51−55.

(35) Elci, A.; Scully, M. O.; Smirl, A. L.; Matter, J. C. Ultrafast transient response of solid-state plasmas. I. Germanium, theory, and experiment. *Phys. Rev. B* **1977**, *16*, 191−221.

(36) Owrutsky, J. C.; Pomfret, M. B.; Brown, D. J. Coherent Acoustic Oscillations of Nanorods Composed of Various Metals. *J. Phys. Chem. C* **2009**, *113*, 10947−10955.

(37) Crut, A.; Maioli, P.; Del Fatti, N.; Vallee, F. Acoustic vibrations of metal nano-objects: Time-domain investigations. *Phys. Rep.* **2015**, *549*, 1−43.

(38) Yan, Y. X.; Gamble, E. B.; Nelson, K. A. Impulsive stimulated scattering: General importance in femtosecond laser pulse interactions with matter, and spectroscopic applications. *J. Chem. Phys.* **1985**, *83*, 5391−5399.

(39) Fu, Z.; Yamaguchi, M. Coherent Excitation of Optical Phonons in GaAs by Broadband Terahertz Pulses. *Sci. Rep.* **2016**, *6*, 38264.

(40) Chang, Y. M.; Chuang, C. T.; Chia, C. T.; Tsen, K. T.; Lu, H.; Schaff, W. J. Coherent longitudinal optical phonon and plasmon coupling in the near-surface region of InN. *Appl. Phys. Lett.* **2004**, *85*, 5224−5226.

(41) Shalini, A.; Liu, Y.; Al-Jarah, U. A.; Srivastava, G. P.; Wright, C. D.; Katmis, F.; Braun, W.; Hicken, R. J. Observation of T(2)-like coherent optical phonons in epitaxial Ge(2)Sb(2)Te(5)/GaSb(001) films. *Sci. Rep.* **2013**, *3*, 2965.

(42) Cho, G. C.; Kutt, W.; Kurz, H. Subpicosecond time-resolved coherent-phonon oscillations in GaAs. *Phys. Rev. Lett.* **1990**, *65*, 764−766.

(43) Wright, O. B.; Perrin, B.; Matsuda, O.; Gusev, V. E. Ultrafast carrier diffusion in gallium arsenide probed with picosecond acoustic pulses. *Phys. Rev. B: Condens. Matter Mater. Phys.* **2001**, *64*, 81202 DOI: 10.1103/PhysRevB.64.081202.

(44) Thomsen, C.; Grahn, H. T.; Maris, H. J.; Tauc, J. Surface generation and detection of phonons by picosecond light pulses. *Phys. Rev. B: Condens. Matter Mater. Phys.* **1986**, *34*, 4129−4138.

(45) Nelson, K. A.; Fayer, M. D. Laser induced phonons: A probe of intermolecular interactions in molecular solids. *J. Chem. Phys.* **1980**, *72*, 5202−5218.

(46) Ouyang, G.; Zhu, W. G.; Sun, C. Q.; Zhu, Z. M.; Liao, S. Z. Atomistic origin of lattice strain on stiffness of nanoparticles. *Phys. Chem. Chem. Phys.* **2010**, *12*, 1543−9.

(47) Ruello, P.; Gusev, V. E. Physical mechanisms of coherent acoustic phonons generation by ultrafast laser action. *Ultrasonics* **2015**, *56*, 21−35.

(48) Maycock, P. D. Thermal conductivity of silicon, germanium, III−V compounds and III−V alloys. *Solid-State Electron.* **1967**, *10*, 161−168.

(49) Auston, D. H.; Shank, C. V. Picosecond Ellipsometry of Transient Electron-Hole Plasmas in Germanium. *Phys. Rev. Lett.* **1974**, *32*, 1120−1123.

(50) Hsiao, T. K.; Huang, B. W.; Chang, H. K.; Liou, S. C.; Chu, M. W.; Lee, S. C.; Chang, C. W. Micron-scale ballistic thermal conduction and suppressed thermal conductivity in heterogeneously interfaced nanowires. *Phys. Rev. B: Condens. Matter Mater. Phys.* **2015**, *91*, 35406 DOI: 10.1103/PhysRevB.91.035406.

(51) Smith, R. C. High-Temperature Specific Heat of Germanium. *J. Appl. Phys.* **1966**, *37*, 4860−4865.

(52) McCarthy, K. A.; Ballard, S. S. Thermal Conductivity of Germanium at Ambient Temperatures. *Phys. Rev.* **1955**, *99*, 1104−1104.

(53) Léonard, F.; Talin, A. A.; Swartzentruber, B. S.; Picraux, S. T. Diameter-Dependent Electronic Transport Properties of Au-Catalyst/Ge-Nanowire Schottky Diodes. *Phys. Rev. Lett.* **2009**, *102*, 106805.

(54) Young, J. F.; van Driel, H. M. Ambipolar diffusion of high-density electrons and holes in Ge, Si, and GaAs: Many-body effects. *Phys. Rev. B: Condens. Matter Mater. Phys.* **1982**, *26*, 2147−2158.

(55) Othonos, A.; van Driel, H. M.; Young, J. F.; Kelly, P. J. Correlation of hot-phonon and hot-carrier kinetics in Ge on a picosecond time scale. *Phys. Rev. B: Condens. Matter Mater. Phys.* **1991**, *43*, 6682−6690.

(56) Greaves, G. N.; Greer, A. L.; Lakes, R. S.; Rouxel, T. Poisson's ratio and modern materials. *Nat. Mater.* **2011**, *10*, 823−37.

(57) Jerebtsov, S. N.; Kolomenskii, A. A.; Liu, H.; Zhang, H.; Ye, Z.; Luo, Z.; Wu, W.; Paulus, G. G.; Schuessler, H. A. Laser-excited acoustic oscillations in silver and bismuth nanowires. *Phys. Rev. B: Condens. Matter Mater. Phys.* **2007**, *76*, 184301 DOI: 10.1103/PhysRevB.76.184301.

(58) Wolff, C.; Soref, R.; Poulton, C. G.; Eggleton, B. J. Germanium as a material for stimulated Brillouin scattering in the mid-infrared. *Opt. Express* **2014**, *22*, 30735−47.

(59) Belliard, L.; Cornelius, T. W.; Perrin, B.; Kacemi, N.; Becerra, L.; Thomas, O.; Eugenia Toimil-Molares, M.; Cassinelli, M. Vibrational response of free standing single copper nanowire through transient reflectivity microscopy. *J. Appl. Phys.* **2013**, *114*, 193509.

(60) Major, T. A.; Crut, A.; Gao, B.; Lo, S. S.; Del Fatti, N.; Vallee, F.; Hartland, G. V. Damping of the acoustic vibrations of a suspended gold nanowire in air and water environments. *Phys. Chem. Chem. Phys.* **2013**, *15*, 4169−76.

(61) Kim, C.-J.; Lee, H.-S.; Cho, Y.-J.; Kang, K.; Jo, M.-H. Diameter-Dependent Internal Gain in Ohmic Ge Nanowire Photodetectors. *Nano Lett.* **2010**, *10*, 2043−2048.

(62) Cavalleri, A.; Schoenlein, R. W. Femtosecond X-Rays and Structural Dynamics in Condensed Matter. In *Ultrafast Dynamical Processes in Semiconductors;* Tsen, K.-T., Ed.; Springer Berlin Heidelberg: Berlin, Germany, 2004; pp 309−338.